Ninth Canadian Conference on Earthquake Engineering
Ottawa, Ontario, Canada
26-29 June 2007

SEISMICALLY INDUCED SHEAR DISPLACEMENTS IN REPOSITORY HOST ROCK FRACTURES

B. Fälth[1], H. Hökmark[2] and R. Munier[3]

ABSTRACT

The Swedish Nuclear Fuel and Waste Management Company (SKB) will apply the KBS-3 system for disposal of spent nuclear fuel. The fuel will be encapsulated in canisters which will be deposited in vertical deposition holes in crystalline rock at 500 m depth. In the safety assessment, SKB considers the possibility of large earthquakes in connection with future glacial cycles. The main concern is that such earthquakes may induce slip along fractures intersecting deposition holes and that the slip is sufficiently large to jeopardize the integrity of the canister. This paper presents an attempt to simulate a rupture along a potentially unstable fault and to study the static and dynamic effects on nearby and distant fractures. Dynamic 3D-models, including an earthquake fault as well as numerous surrounding fractures, were analyzed to examine the scope and extent of induced fracture slip. The model geometry, the mechanical properties of fault and rock, and the in-situ stresses were calibrated to give a seismic moment corresponding to a magnitude 6 event. An algorithm was developed to initiate the rupture at the hypocenter and control the rupture propagation along the fault plane.

Introduction and Background

The concept for spent nuclear fuel disposal applied by the Swedish Nuclear Fuel and Waste Management Company (SKB) is the KBS-3 system (SKB 2006a). The spent fuel will be encapsulated in canisters consisting of a cast iron insert surrounded by a copper shell. The canisters will be deposited in vertical deposition holes in crystalline rock at approximately 500 m depth and surrounded by a barrier of bentonite clay for isolation and mechanical protection. The fuel will be hazardous for a very long time and the time perspectives applied in the safety assessment work is hundreds of thousands of years. Within this time span, the repository is likely to be subjected to effects of future glaciations (SKB 2006a).

There is evidence that intensive seismic activity, postglacial faulting, took place in Northern Sweden in direct conjunction with the melting of the most recent ice cap (e.g. the Lansjärv Fault, the Parvie Fault) (Arvidsson 1996). The magnitude of the Lansjärv earthquake, for instance, is estimated to have been 7.8 (Muir Wood 1993). The possibility that post-glacial seismic activities along existing faults can induce slip along fractures at some distance from the rupturing fault is considered in SKB's safety assessment. From the safety assessment point of view the concern is that such slipping fractures may intersect a deposition hole such that the consequent canister shear deformation results in canister damage. Potentially this

[1]M.Sc. Mechanical Engineering, Clay Technology AB, IDEON Research Center, Scheelevägen 19F, SE-223 70 Lund, Sweden
[2]M.Sc. Physics, Clay Technology AB, IDEON Research Center, Scheelevägen 19F, SE-223 70 Lund, Sweden
[3]Ph.D. Structural Geology, Svensk Kärnbränslehantering AB, Box, 5864, SE-102 40 Stockholm, Sweden

might reduce the isolation capacity of the canister and jeopardize the integrity of the barrier system. According to the present-day canister damage criterion applied by SKB, fracture slip exceeding 0.1 m across deposition holes count as canister damage (SKB 2006a).

The problem discussed above has been addressed previously by for instance Munier and Hökmark (2004). They reported modeling results from models where the fractures were arbitrarily and conservatively assumed to be frictionless or to have low shear strength. In the present study, fracture shear strength parameter values based on site investigation data were used. The modeling approach and the results presented in this paper are described in detail by Fälth and Hökmark (2006).

Objective

The objective of this work was to investigate the static and dynamic impact of an earthquake on nearby fractures in terms of induced slip and to compare the amount of slip with the canister damage criterion. The correlation between the induced slip movements and the distance from the source was also to be examined.

Modeling Approach

The objective of the work was addressed by analysis of numerical models set up according to the following:

- A seismic dip-slip event takes place in a pre-existing, steeply dipping fault. The fault is of reverse type, as proposed for glacially induced faults observed in northern Fennoscandia (Muir Wood 1993).
- The earthquake is of magnitude 6 or larger.
- The fault may either
    a. have a blind upper termination, i.e. its upper edge is located below the ground surface or
    b. breach the ground surface.
- At about 500 m depth, fractures are located at different distances from the fault.

Two models were created and analyzed by use of 3DEC, which is a three-dimensional code based on the distinct element method (Itasca 2003). A large discontinuity representing a preexisting potential earthquake fault (the primary fault) and a number of smaller discontinuities (target fractures) were defined. The small discontinuities represented fractures in which slip potentially may be induced by the earthquake. In-situ stresses were applied and a rupture was initiated and programmed to propagate along the plane of the primary fault, resulting in fault slip and accompanying strain energy release. This approach made it possible to study the target fracture slip induced by static stress redistribution as well as by dynamic oscillations. The two models had different fault geometries (Fig. 1). In Case A, the upper edge of the primary fault was located 1000 m below the ground surface. Case B was similar to Case A, but with the primary fault breaching the ground surface.

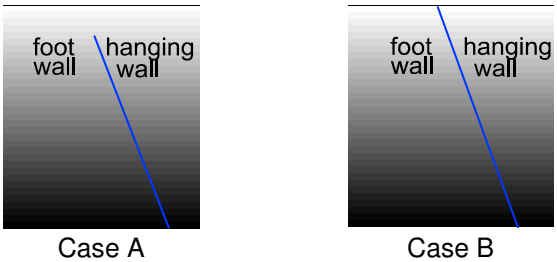

Figure 1. Case A with buried rupture and Case B with rupture breaching the ground surface.

In Fig. 2, a model overview is shown along with the model dimensions. The upper boundary of the models represented the ground surface and the target fractures were located at 500 m depth. Since larger displacements were expected in the Case B model, this model had larger dimensions than Case A. The

fault length was 4 km, but since the boundary at z = 0 was a symmetry plane the models simulated an actual fault length of 8 km. The orthogonal cuts seen in the figure correspond to mechanically invisible construction planes used to define the geometry and to facilitate the discretization of the continuum.

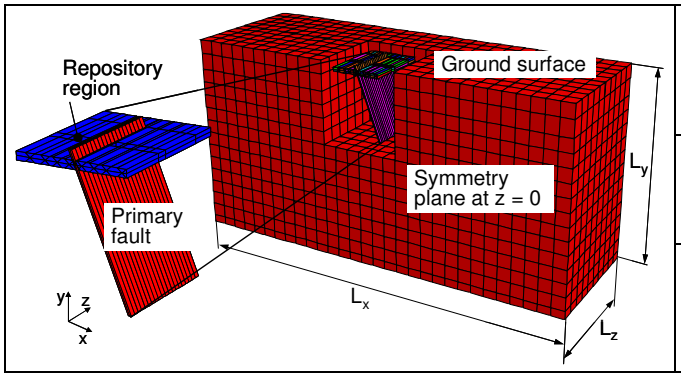

Case	L_x	L_y	L_z	Primary fault dimensions (length x width)	Unit
A	16	9	8	4 x 4.6	km
B	30	15	10	4 x 5.6	km

Figure 2. Geometry outlines and model dimensions. The picture relates to Case B.

Numerous target fractures, all with 150 m radii, located at different distances from the primary fault and at different distances from the symmetry plane, were included at 500 m depth. The fractures were defined by assigning "real" fracture properties to circular areas of 3DEC cut planes. The remainders of the cut planes were assigned with fictitious fracture properties that prevented slip. Horizontal target fractures as well as target fractures dipping 45º were defined. Fig. 3 (left) shows the planes of the target fractures and the plane of the steeply dipping primary fault. The right picture shows the target fracture locations and dip directions. Two dip directions were used: 90° (same as the fault, i.e. along the positive x-axis) and dip direction 270° (along negative x-axis). The dotted line indicates the intersection of the primary fault with the viewing plane at 500 m depth.

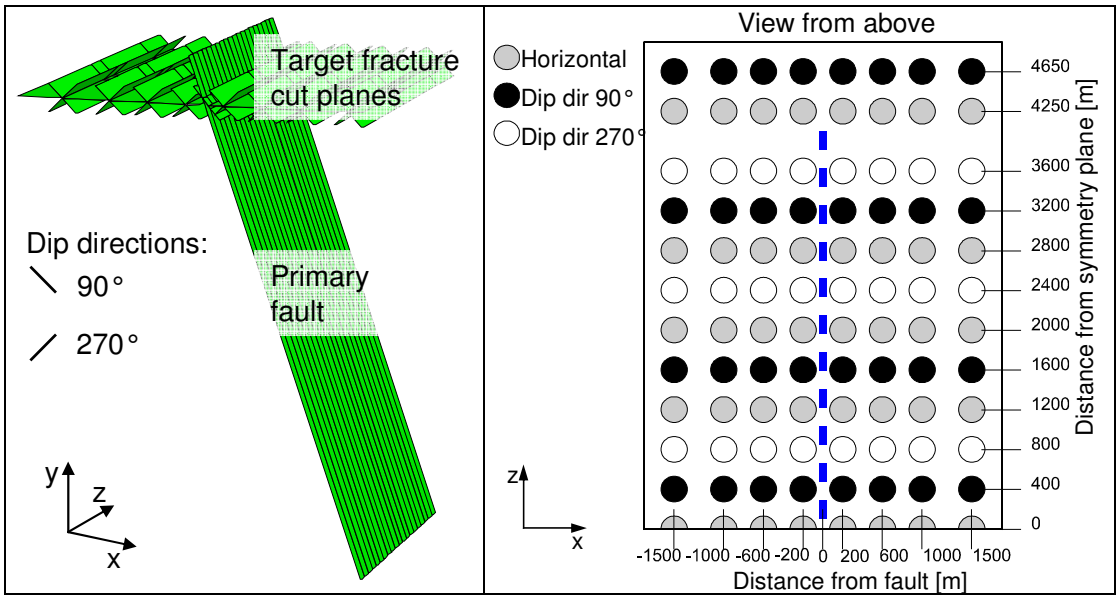

Figure 3. Left: 3DEC cut planes in which the circular target fractures were defined. The primary fault with dip direction 90° is also shown. Right: Explanatory sketch of the target fracture locations and dip directions. Fractures are shown as circles, irrespective of dip.

The continuum was assumed to be linearly elastic with generic parameter values; Young's modulus $7.5 \cdot 10^{10}$ Pa, Poisson's ratio 0.25 and density 2700 kg/m^3. The fractures responded to loads according to

an idealized elasto-plastic material model with linear joint stiffness, zero tensile strength and shear failure according to a Coulomb criterion. The parameter values for the discontinuities are presented in Table 1.

Table 1. Material property parameter values for the discontinuities.

Component	**Friction angle (deg)**	**Cohesion c ($\cdot 10^6$ Pa)**	**Tensile strength (Pa)**	**Normal stiffness ($\cdot 10^9$ Pa/m)**	**Shear stiffness ($\cdot 10^9$ Pa/m)**
Primary fault	0	0 (after completed rupture)	0	10	10
Target fractures	34*	0.5*	0	10	10

* Value in accordance with site investigation data (SKB 2005a; SKB 2005b; SKB 2006b).

The initial stresses were set according to Fig. 4, left. This gave fault shear stresses that increased linearly with depth with an average value of about $1.5 \cdot 10^7$ Pa (right). A constant $5 \cdot 10^6$ Pa pore pressure was set in all fractures giving a corresponding reduction of the effective stress. The simulations comprised two main phases: A static phase and a dynamic phase (Fig. 5). All vertical boundaries and the bottom boundary were fixed in the normal direction during the static phase. During the dynamic phase, these boundaries (except the symmetry boundary at z = 0) were redefined as non-reflecting (viscous) boundaries. The top boundary was free, allowing for surface reflections.

Component	Value ($\cdot 10^6$ Pa)	Comment
σ_x	17.25+0.0361·Y	Perpendicular to primary fault strike
σ_y	0.0265·Y	Vertical stress
σ_z	4.31+0.0156·Y	Parallel to primary fault strike
$\sigma_{xy}=\sigma_{xz}=\sigma_{yz}$	0	

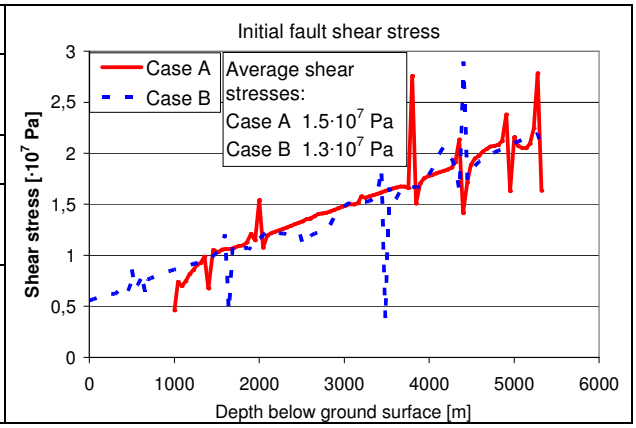

Figure 4. Left: Initial stresses as function of depth (Y). Right: The diagram shows initial shear stress versus depth in the fault. The stress peaks are anomalies appearing at block edges and have no importance for the results.

During the static phase, static equilibrium was established under the initial stresses. The cohesive strength assigned to the primary fault was high enough to prevent slip. During the dynamic phase, a scheme for rupture initiation and propagation was applied. The parameter values which were used are presented in Fig. 6. The rupture was initiated at 3160 m depth and was programmed to move outwardly in the radial direction along the primary fault. At every time step, the cohesive strength of each sub-contact in the fault was updated to match the shear stress currently acting at that particular location. After rupture front arrival, the shear strength was ramped down to zero over a period of 0.5 seconds. The zero residual shear strength in the primary fault resulted in a net stress drop equal to the initial shear stress, i.e. about $1.5 \cdot 10^7$ Pa on average (Fig. 4, right). This is consistent with stress drop values suggested for intra-plate earthquakes (Scholz 1990). The definition of circular target fracture areas as well as the rupture initiation and propagation were managed using the built-in programming language FISH (Itasca 2003).

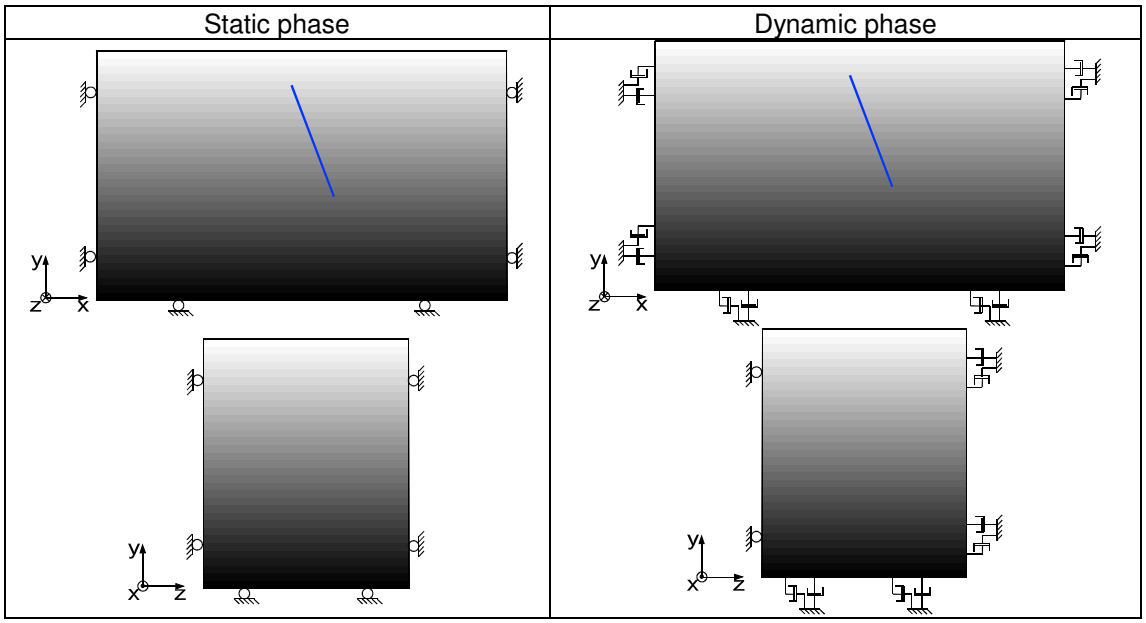

Figure 5. Boundary conditions. Roller boundaries (except at symmetry plane, z=0) were switched to viscous (non-reflecting) boundaries during the dynamic phase.

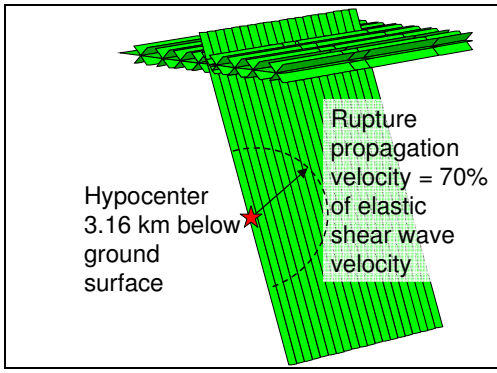

Parameter values

- Hypocenter location: At 3.16 km depth at z = 0
- Rupture propagation velocity: 2333 m/s (70% of the rock mass shear wave velocity)
- Rise time: 0.5 s (time used to complete the rupture at each location at the fault)

Figure 6. Left: Location of the hypocenter and propagation of the rupture. The figure also shows the cut planes where target fractures were located. Right: Parameter values.

Results

Fig. 7 (left) shows the primary fault shear stress as function of time at four points at hypocenter depth in Case B. The curves illustrate how the rupture front propagates outwardly from the hypocenter; the shear stress reduction starts at different instances of time at different locations. It is also shown how the shear strength is ramped down during about 0.5 seconds at each location. To the right, the primary fault slip histories for the same four points are shown. The slip starts at different times, which is in accordance with the stress results shown in the left diagram.

Fig. 8 shows vector plots of the slip along the primary fault at three instances of time. The rupture initiation at the hypocenter and the radial rupture propagation are lucidly illustrated. It takes about 1 second for the rupture in Case A to reach the horizontal fault edges, which is in agreement with the specified rupture propagation velocity. As expected, the primary fault slip was considerably larger in Case B than in Case A. In Case A, the maximum resulting fault slip was 1.9 m and the moment magnitude, M_w, was 6.0. The

corresponding numbers for Case B were 3.0 m and 6.2, respectively. The maximum slip was found close to the hypocenter in Case A and close to the ground surface in Case B.

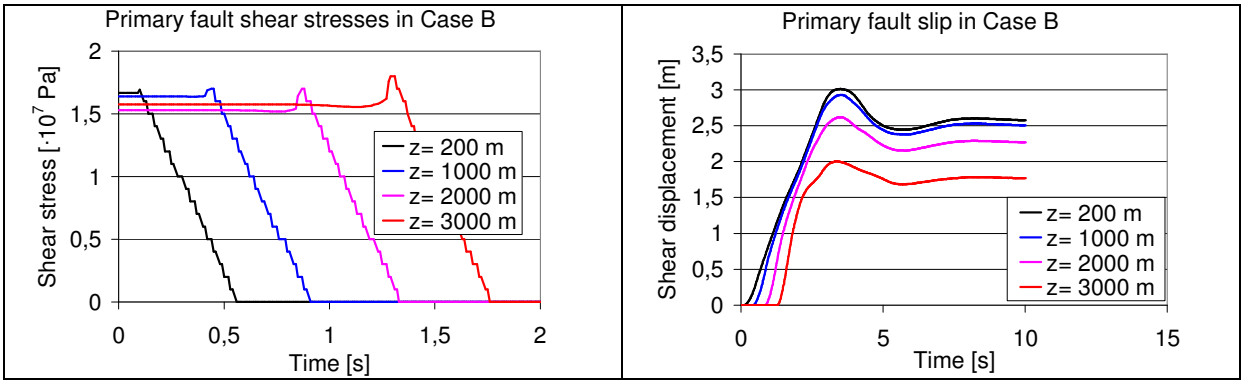

Figure 7. Fault shear stress (left) and slip (right) as function of time for four points at hypocenter depth.

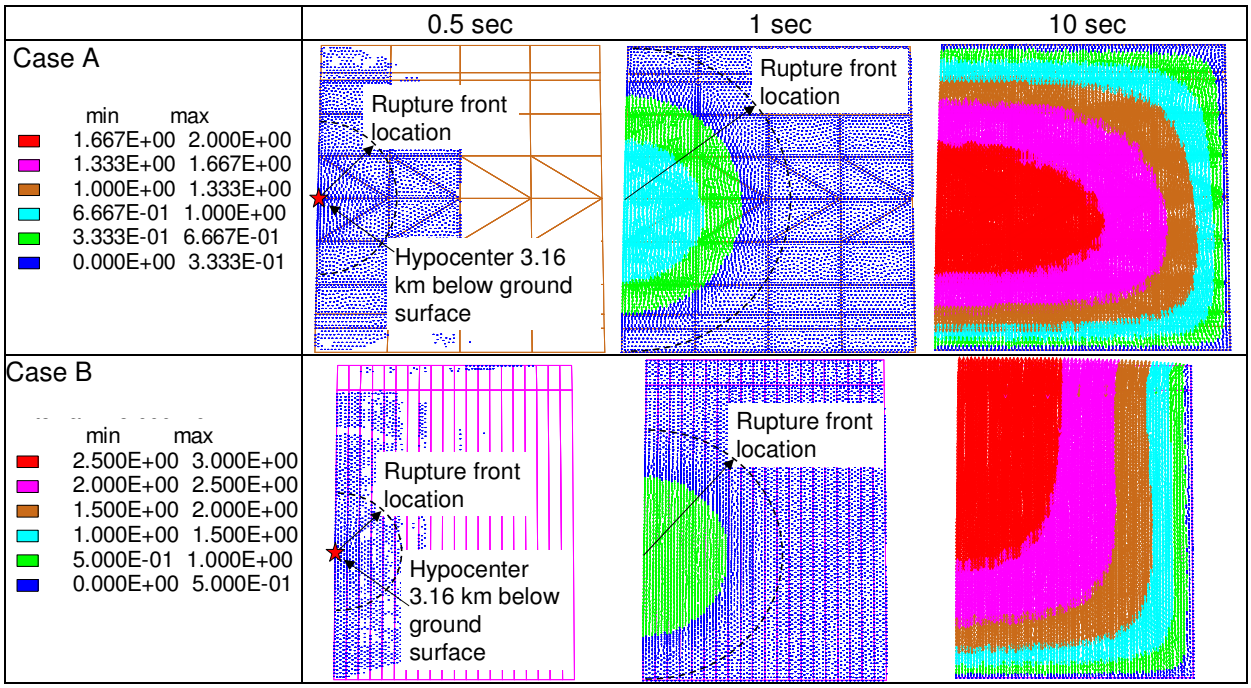

Figure 8. Shear displacement vectors showing slip along primary fault at three instances of time.

The amount of induced target fracture slip is the key output parameter from the models which should be compared with the 0.1 m canister damage criterion applied by SKB (SKB 2006a). Fig. 9 (left) shows an overview of the induced peak target fracture slip. The grey-scale indicates the target fracture dip direction and the thick lines indicate the location of the primary fault. In Case A, the fault ended 500 m below the repository level and the dashed line indicates the intersection between the repository level and the extension of the fault. In Case B, the fault intersected the repository level. The different fault geometries gave different patterns of deformation and stress redistribution in the rock mass. This is visible in the difference in target fracture slip results. The maximum slip in Case A was 46 mm and was found in a fracture with dip direction 90° located at z = 400 m. In Case B, the maximum slip (58 mm) was found in a fracture with dip direction 270° located close to the vertical fault edge at z ~ 4000 m. In general, the fracture slip close to the vertical fault edge was significantly larger in Case B than in Case A.

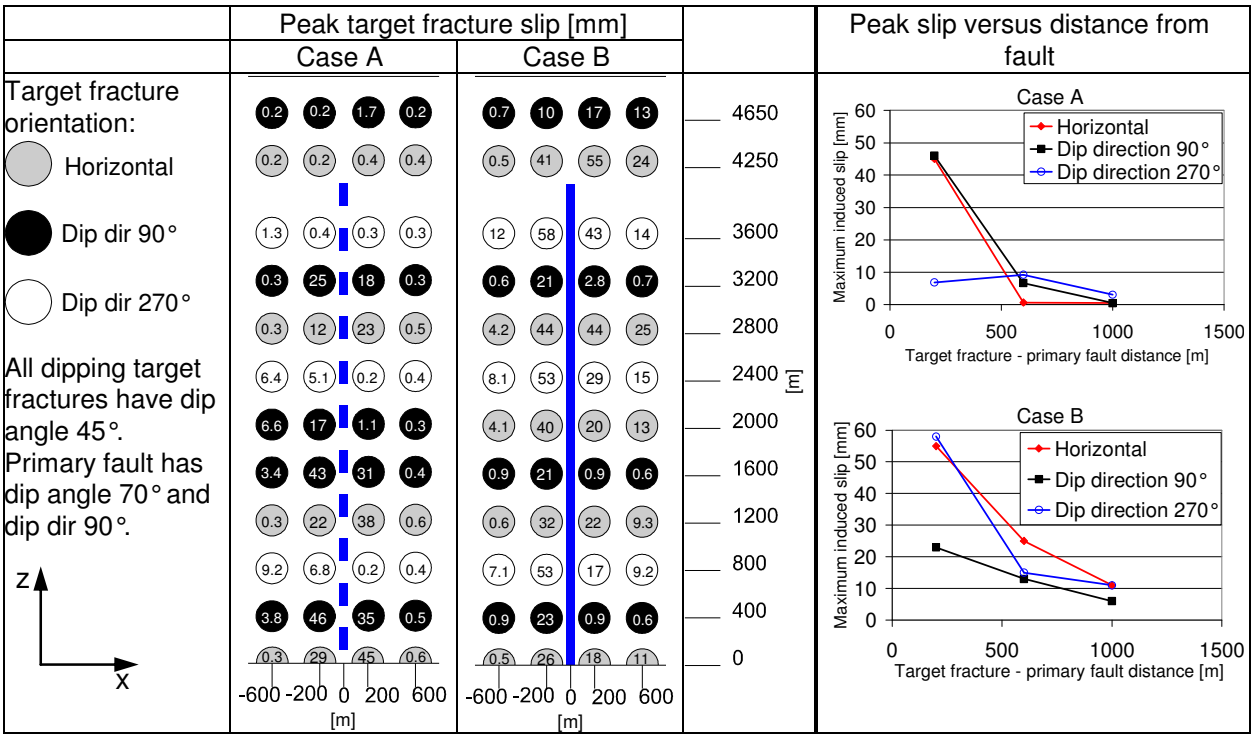

Figure 9. Left: Peak slip in target fractures at 200 m and 600 m distance from primary fault. Right: Maximum target fracture peak slip versus distance from the primary fault.

The diagrams in Fig. 9 (right) show how the peak target fracture slip depends on the distance from the primary fault. The peak slip is significantly smaller at 600 m distance than at 200 m, except for one type of fracture in Case A. The peak slip of the 270° dip direction fractures is slightly larger at 600 m than at 200 m. The diagrams also illustrate how the amount of slip differs between fractures with different orientations depending on the primary fault geometry.

Fig. 10 (left) is a Mohr's circle diagram which shows the stress states at 200 m distance from the fault and at 600 m distance from the symmetry plane before and after the earthquake. The dotted line is the failure envelope for fractures with friction angle 34° and cohesion $0.5 \cdot 10^6$ Pa. The black semi-circle representing the stress state before the earthquake indicates that all fractures are stable, irrespective of dip. After the earthquake, the major principal (horizontal) stress at the foot wall side in Case A has increased and the minor principal stress (vertical) has decreased such that the shear stress exceeds the stability limit within a 50° dip range. At the hanging wall side all fractures are stable also after the earthquake. The stress states found in Case B after the earthquake indicate that fractures are more stable after the earthquake than before. However, even in cases where the change in static stress state would increase the stability, the target fractures were found to slip. This shows that the dynamic effects are important for the target fractures slip.

Fig. 10 (right) shows the shear and effective normal stresses on a 45° dipping plane located 200 m from the fault and 600 m from the symmetry plane in Case B. The stresses were recorded at a point located between two target fractures (i.e. no slip possible at this point). Along with the stress curves there is also a curve that shows the shear strength variation for a hypothetical fracture at that location. The shear strength is a function of the normal stress σ_n and was calculated as $c+\sigma_n\tan(\alpha) = 0.5 \cdot 10^6 + \sigma_n \tan(34°)$ Pa. The following can be observed:

- The stability margin is larger after the earthquake than before. This is in agreement with the results shown in Fig. 10 (left).
- Between 1.25 and 1.5 s after rupture initiation, there is an increase in acting shear stress and a

simultaneous decrease in normal stress. The decrease in normal stress reduces the shear strength which drops below the acting shear stress for a little less than half a second. During that time a fracture at this location would slip. This indicates that dynamic stress oscillations are important for inducing target fracture slip, and that dynamic effects may trigger slip also in fractures that would be stable under the static stress state.

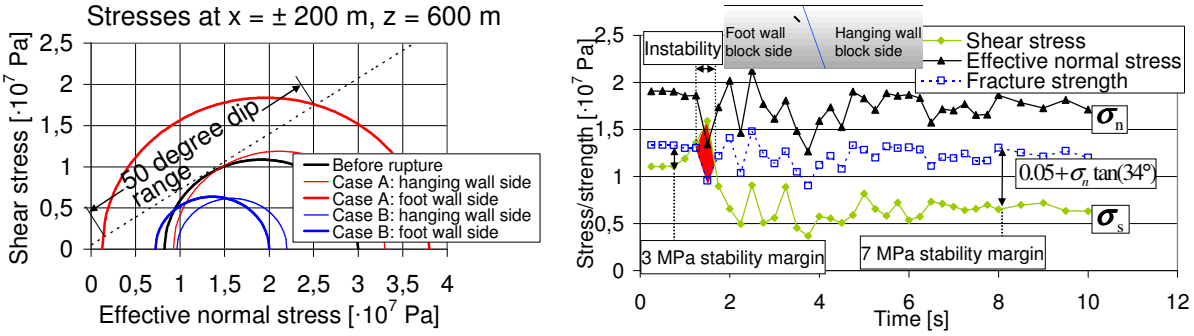

Figure 10. Left: Mohr's circle diagram illustrating static stress states before and after earthquake. Right: Shear stress and shear strength at cut plane between fractures in Case B. The red area indicates a period of instability.

Discussion

The models analyzed here were developed to simulate magnitude 6 earthquakes in a schematic and robust way and to study possible impacts on a number of neighboring target fractures. The aim was to generate reasonably realistic and conservative dynamic stress waves and changes in the static stress state. The models did not, however, capture the complexity related to, for instance, the distribution of fault surface asperities or to any spatial variability in mechanical properties. No attempts were made to assess the possible effects of a fractured transition zone between the actual slip plane and the undisturbed rock mass. The importance of these idealizations should be examined as part of the continued work.

The amount of target fracture slip found in the models analyzed here is smaller than those found in previous studies (Munier and Hökmark 2004), where more conservative target fracture strength assumptions were made. The modeling results reported by Munier and Hökmark (2004) were based on conservative assumptions regarding target fracture shear strength. The fractures in that study were arbitrarily and conservatively assumed to be frictionless or to have a low friction angle (15°) whereas the 34° friction angle used in the present study is based on site data (SKB 2005a; SKB 2005b; SKB 2006b). Thus, the shear strength parameter values used here can be assumed to be more realistic. However, these values are based on results from static tests performed on small-scale samples. There are some uncertainties of how relevant these values are for the target fractures, which are subjected to dynamic loads and have radii of hundreds of meters. A constant $0.5 \cdot 10^6$ Pa pore pressure was specified for all target fractures, without any attempts to consider effects of possible pore pressure transients. Also the importance of some of these idealizations should be examined in future analyses.

Fig. 11 shows data base regressions which relate rupture area and average faults displacement to moment magnitude (Wells and Coppersmith 1994). Data from the Case A model are indicated with stars in the diagrams. To the left, the correlation between magnitude and rupture area is shown. The rupture area in the model is about half the average area reported for reverse type events. The average primary fault slip (1.2 m) in Case A is about 10 times larger than the average slip suggested for magnitude 6 events (Fig. 11, right). In Case B, the average slip was even larger (1.9 m). Thus, the stress drop, the particle velocity (velocity of rock close to fault) and consequently the stress wave amplitudes are likely to have been overestimated in comparison with typical average events. This suggests that the calculated effects on target fractures are on the conservative side. However, the data base regressions do not regard glacially induced earthquakes.

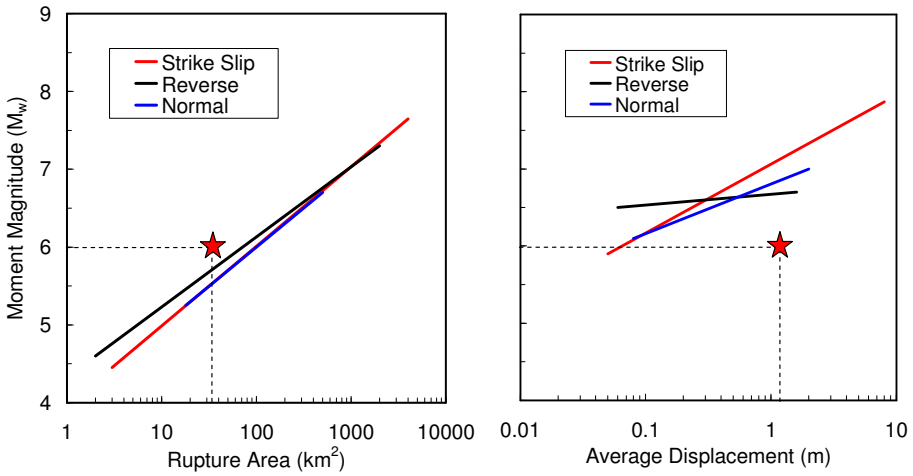

Figure 11. Database regressions of the correlation between (left) moment magnitude and rupture area and (right) moment magnitude and fault average displacement (Wells and Coppersmith 1994). Data from the Case A model are indicated with stars in the figure.

According to the present results, fractures with 150 m radius can be allowed to intersect deposition holes at 200 m distance from potential earthquake faults capable of hosting earthquakes of at least magnitude 6 without risk of any seismically induced canister damage. Further work will, however, examine the effects of larger earthquakes. A larger earthquake will have a larger range of influence compared with the magnitude 6 earthquakes considered here, i.e. target fracture slip are not likely to decrease with distance as rapidly as illustrated in Fig. 9 (right). The response of nearby target fractures, however, is not determined by the total amount of released strain energy, but by the behavior of nearby parts of the earthquake fault. Therefore there is a possibility that the behavior of target fractures located close to the fault can be similar to the behavior found here. As far as effects of the static stress redistribution are concerned, this is likely to be the case provided that the stress drop can be assumed to be independent of magnitude as suggested by Scholz (1990). The present results indicate, however, that the dynamic effects are important for triggering target fracture slip. Even if the average static stress drop is equal to what was used here for magnitude 6 earthquakes, the fault slip velocity may be higher, which would give higher stress wave amplitudes and, potentially, more target fracture slip. If this issue should be regarded as a real concern is, however, uncertain. Therefore, target fracture slip caused by M 7 and M 8 earthquakes should be calculated.

Conclusions

This paper presents a method to predict or estimate the amount of shear slip that can be induced in a fracture by a seismic event in a neighbouring preexisting fault. The method was based on the dynamic logic and the built-in programming facilities of the three-dimensional distinct element code 3DEC. A rupture was initiated in a potentially unstable fault and programmed to propagate with a specified rupture velocity and with a specified rise time. The initial stresses were calibrated to yield the intended stress drop, fault slip and magnitude. The combined static and dynamic effects on a number of explicitly modeled target fractures were studied. The induced target fracture slip was recorded and compared with the canister damage criterion which is currently applied in the SKB safety assessment work.

Two magnitude 6 earthquakes with different fault geometries were simulated. The largest induced target fracture slip was found 200 m from the earthquake fault in the model where the rupture breached the ground surface. The largest slip was 0.058 m, i.e. well below the 0.1 m canister damage criterion applied by SKB. Further, the results confirmed that the distance between the primary fault and the target fracture has a great importance for the amount of induced slip. At 600 m distance, the maximum target fracture

slip was less than half that found at 200 m. At larger distances, the maximum fracture slip was even smaller.

The results illustrated that there are two possible fracture slip mechanisms. In regions around fault edges, the change in the static stress state alone may be sufficient to generate slip. In regions where the effect of the strain energy release is to relax stresses and increase the fracture stability, slip may be triggered by stress peaks and temporary strength reductions.

Acknowledgements

The authors wish to acknowledge that this paper is a result of work funded by the Swedish Nuclear Fuel and Waste Management Company (SKB).

References

Arvidsson, R., 1996. Fennoscandian Earthquakes: Whole Crustal Rupturing Related to Postglacial Rebound. *Science* 274, 744-746.

Fälth, B., and Hökmark H., 2006. Seismically induced slip on rock fractures. Results from dynamic discrete fracture modeling. *SKB R-06-48.* Svensk Kärnbränslehantering AB, Stockholm. (www.skb.se).

Itasca Consulting Group Inc., 2003. *3DEC – 3-Dimensional Distinct Element Code, User's Guide,* Minneapolis, USA.

Muir Wood, R., 1993. A review of the seismotectonics of Sweden. *SKB TR-93-13.* Svensk Kärnbränslehantering AB, Stockholm.

Munier, R., and Hökmark H*.,* 2004. Respect distances. Rationale and means of computation. *SKB R-04-17.* Svensk Kärnbränslehantering AB, Stockholm. (www.skb.se).

Scholz, C. H., 1990. *The mechanics of earthquakes and faulting*. Cambridge University Press, United Kingdom.

SKB, 2005a. Preliminary site description. Simpevarp subarea – version 1.2. *SKB R-05-08.* Svensk Kärnbränslehantering AB, Stockholm. (www.skb.se).

SKB, 2005b. Preliminary site description. Forsmark area – version 1.2. *SKB R-05-18.* Svensk Kärnbränslehantering AB, Stockholm. (www.skb.se).

SKB, 2006a. Long-term safety for KBS-3 repositories at Forsmark and Laxemar – a first evaluation. *SKB TR-06-09.* Svensk Kärnbränslehantering AB, Stockholm. (www.skb.se).

SKB, 2006b. Preliminary site description. Laxemar subarea – version 1.2. *SKB R-06-10.* Svensk Kärnbränslehantering AB, Stockholm. (www.skb.se).

Wells, D. L., and Coppersmith K. J., 1994. New empirical relationships among magnitude, rupture length, rupture width, rupture area, and surface displacement. *Bulletin of the Seismological Society of America* 84 (4), 974–1002.